Published in final edited form as:
Cardiovasc Intervent Radiol. 2015 February ; 38(1): 182–190. doi:10.1007/s00270-014-0905-2.

Planning Irreversible Electroporation (IRE) in the Porcine Kidney: Are Numerical Simulations Reliable for Predicting Empiric Ablation Outcomes?

Thomas Wimmer, MD[1,2], **Govindarajan Srimathveeravalli, PhD**[1], **Narendra Gutta, MD**[1], **Paula C. Ezell, DVM**[3], **Sebastien Monette, DVM, MVSc**[4], **Majid Maybody, MD**[1], **Joseph P. Erinjery, MD, PhD**[1], **Jeremy C. Durack, MD**[1], **Jonathan A. Coleman, MD**[5], and **Stephen B. Solomon, MD**[1]

[1]Interventional Radiology Service, Department of Radiology, Memorial Sloan-Kettering Cancer Center, New York, NY

[2]Division of General Radiology, Department of Radiology, Medical University of Graz, Graz, Austria

[3]Research Animal Resource Center, Memorial Sloan-Kettering Cancer Center, Weill Cornell Medical College, The Rockefeller University, New York, NY

[4]Laboratory of Comparative Pathology, Memorial Sloan-Kettering Cancer Center, Weill Cornell Medical College, The Rockefeller University, New York, NY

[5]Urology Service, Department of Surgery, Memorial Sloan-Kettering Cancer Center, New York, NY

Abstract

Purpose—Numerical simulations are used for treatment planning in clinical applications of irreversible electroporation (IRE) to determine ablation size and shape. To assess the reliability of simulations for treatment planning, we compared simulation results with empiric outcomes of renal IRE using computed tomography (CT) and histology in an animal model.

Materials and Methods—The ablation size and shape for 6 different IRE parameter sets (70–90 pulses, 2000–2700V, 70–100μs) for monopolar and bipolar electrodes was simulated using a numerical model. Employing these treatment parameters 35 CT-guided IRE ablations were created in both kidneys of 6 pigs and followed-up with CT immediately and after 24 hours. Histopathology was analyzed from post-ablation day 1.

Results—Ablation zones on CT measured 81±18% (day 0, $p \leq 0.05$) and 115±18% (day 1, $p \leq 0.09$) of the simulated size for monopolar electrodes, 190±33% (day 0, $p \leq 0.001$) and 234±12%

Correspondence to: Dr. Thomas Wimmer, Department of Radiology, Medical University of Graz, Austria. Auenbruggerplatz 9, 8036 Graz, Austria. Tel: +43 316 80952, Fax: 212-717-3325, thomas.wimmer@medunigraz.at.

Conflict of Interest

Thomas Wimmer, Govindarajan Srimathveeravalli, Narendra Gutta, Paula C. Ezell, Sebastien Monette, Majid Maybody, Joseph P. Erinjery, Jeremy C. Durack, and Jonathan A. Coleman have no conflict of interest. The institution of S. B. Solomon received an unrestricted grant and equipment from Angiodynamics Inc. S. B. Solomon is also a consultant for Covidien and received a grant from GE Healthcare.

(day 1, p≤0.0001) for bipolar electrodes. Histopathology indicated smaller ablation zones than simulated (71±41%, p≤0.047) and measured on CT (47±16%, p≤0.005) with complete ablation of kidney parenchyma within the central zone and incomplete ablation in the periphery.

Conclusions—Both numerical simulations for planning renal IRE and CT measurements may overestimate the size of ablation when compared to histology and ablation effects may be incomplete in the periphery.

Introduction

Nephron-sparing interventions are the current standard for treatment of small renal neoplasms and results from percutaneous ablation techniques are comparable to those of nephron-sparing surgical treatment options in regards of safety and efficacy[1–3]. Relative to surgical alternatives, ablation techniques typically result in fewer complications[4, 5]. Ablation techniques such as radiofrequency ablation (RFA) and cryoablation are increasingly utilized for treating T1a (<4cm) renal masses in patients with higher operative risk. However, thermal ablation close to the collecting system may result in calyceal injury, urine leak, stricture or urinary obstruction[6–8].

Irreversible electroporation (IRE) has emerged as a predominantly non-thermal ablation technique with potential advantages over conventional thermal ablation methods[9]. In IRE, a pulsed direct current electric field is applied via needle electrodes resulting in the breakdown of the cell membrane and finally leading to cell death, as the cell membrane is unable to maintain homeostasis [10, 11]. Wendler et al.[12]and Deodhar et al. [13] have demonstrated that the damage on the urinary collecting system was limited following renal IRE ablation with the potential for urothelium recovery. Wendler et al. [14] have also shown that that IRE in the kidney preserves vascular structures with no observable dysfunction of the kidney perfusion in an ex-vivo model. In a recent publication short- and mid-term effects of renal IRE were evaluated using MRI[15]. Olweny et al. [16] compared histology outcomes of thermal and non-thermal IRE kidney ablations. First clinical studies indicated that IRE is safe in humans for the treatment of renal cell carcinoma[17].

Inter-electrode spacing, electrode exposure, applied voltage, number of pulses and pulse length have been identified as key treatment parameters that influence the ablation shape and size in IRE[18]. Numerical simulations are currently used in clinical applications of IRE to determine the size and shape of the ablation zone for a specific voltage and electrode geometry[18–20]. However, treatment planning on clinically used IRE consoles typically does not consider tissue specific electrical properties. For kidney parenchyma it remains unclear, if treatment planning is able to adequately predict empiric ablation outcomes. We therefore hypothesized that results from simulations for planning IRE ablations may be divergent from empiric outcomes of kidney IRE. We simulated ablations using different treatment parameter sets typically used in clinical applications of IRE and performed IRE ablations in healthy porcine kidneys using similar parameters. CT and histopathology were compared to simulation results to assess the adequacy of simulations.

Materials and Methods

Ablation Model and Simulation

A numerical model was constructed representing treatment planning on clinical consoles. This simulation was used to determine the ablation shape and size for six different treatment parameter sets given in Table 1, dependent on supposed critical electric field strength thresholds for reversible (350V/cm) and irreversible electroporation (600V/cm) [21].

The Laplace equation ($-\nabla.(\sigma\nabla V)$- Equation 1) was solved to determine the electric field distribution. A finite element method (FEM) was used to numerically solve this equation for set boundary conditions using Multiphysics software (Comsol Inc., Burlington, MA). Models of needle electrodes were constructed using AutoCAD Inventor (Autodesk Inc., San Rafael, CA). A cube of 5 cm side-length represented surrounding tissue; conductivity was set to σ=1.0 S/m, which is the value used to represent tissue in the clinically used IRE generator. For monopolar electrodes, one electrode was set to voltage values as described in Table 1, and the other electrode was set to ground. For the bipolar electrode the needle tip was set to positive voltage and the segment above the spacer was set to ground. The boundaries of the tissue block were assumed electrically insulated. Electrodes were embedded into the center of the tissue block, with an electrode spacing as given in Table 1. This geometry was then discretized into a FEM mesh, and numerically solved for determining the electric field distribution resulting from the voltage applied between the electrodes. Detailed information on the construction of the model and numerical simulation can be found in prior work[18, 19, 22].

Animal Model

Under approval of the Institutional Animal Care and Use Committee two to three percutaneous computed tomography (CT)-guided IRE ablations were performed in both kidneys of six Yorkshire pigs (weight range 35–45 kg) provided from one supplier (Archer Farms, Darlington, MD), totaling 35 ablations. All animals were premedicated with tiletamine hydrochloride and zolazepam hydrochloride (Telazol; Fort Dodge Animal Health, Fort Dodge, Iowa; 4.4 mg per kilogram of body weight) administered intramuscularly and after intubation. General anesthesia was maintained with continuous inhalation of 1.5%–3% isoflurane (Baxter, IL) and 100% oxygen on a Penlon Nuffield ventilator. Buprenorphine (0.01 mg/kg) was given via intramuscular injection before the start of each procedure. Rocuronium 1.2 mg/kg was administered intravenously five minutes before performing IRE. Postprocedural pain was managed with intramuscular buprenorphine (0.01 mg/kg) and oral meloxicam (0.4 mg/kg). Animals were euthanized with an intravenous injection of pentobarbital sodium (87 mg/kg) and phenytoin sodium (11 mg/kg; Euthasol; Vibrac AH, Fort Worth, TX).

Interventional Procedure

A pulse generator for clinical application (NanoKnife System, Angiodynamics Inc., Queensbury, NY) was used for irreversible electroporation in all cases. Thirty-five ablations were randomized into 6 different protocols, each consisting of a unique treatment parameter set (Table 1), in accordance with previously reported treatment parameters known to induce

IRE[18, 19]. Three percutaneous ablations were performed in each kidney in the upper, mid and lower pole, with the exception of one kidney where only two ablations in the upper and lower pole were performed due to the presence of a cyst thinning out the underlying cortex. The electrode trajectories were planned on axial CT series (Lightspeed RTLS, GE, Milwaukee, WI) and needle electrodes were inserted under CT guidance exactly in axial plane using the CT laser marker system (Figure 1A, E) after the animals had been anaesthetized and the overlying skin had been shaved and cleansed.

Imaging

Axial multiphase (arterial, venous and delayed phase) contrast enhanced (1.5 cc/kg Iohexol 300; GE Healthcare, Milwaukee, WI) computed tomography (CECT, Light-Speed 16, GE Healthcare, Milwaukee, WI) scans of the abdomen (slice thickness 1.5 mm, reconstruction interval 3 mm) covering both kidneys were acquired immediately and one day post-procedure in all animals to follow-up 35 ablations at each time point. Ablation zones were assessed for contrast enhancement and demarcation as well as size. Size measurements of ablation zones were obtained on a GE Advantage 4.4 workstation from axial CT planes corresponding to the IRE electrode insertion planes. The long (x) and short axis (y) perpendicular and parallel to the electrode insertion tracts were recorded and the cross sectional area was calculated in approximation assuming an elliptical shape ($\pi * x/2 * y/2$ – Equation 2) [23].

Pathology

Kidneys were extracted shortly after euthanasia one day post-intervention. The organs were examined for needle insertion points to identify the ablation zone and sectioned parallel to the needle insertion tracts. Representative sections were fixed in 10% neutral buffered formalin and embedded in paraffin, sectioned at 4 μm thickness, and stained with hematoxylin and eosin (H&E). All specimens were assessed for histopathologic findings consistent with non-thermal or thermal cell injury, cell degeneration and necrosis, inflammatory infiltrates and fibrotic changes.

Size measurements were performed on representative cross sectional histology slides in the plane of the needle insertion tracts. The axis parallel and perpendicular to the electrode was recorded.

Statistics

Statistical comparison between simulated and measured ablation size was done using Wilcoxon’s test for paired samples using IBM SPSS Statistics 21 (IBM corporation, Armonk, NY). Differences were considered significant, if p-values were below 0.05. In tables means and standard deviations are given. In figures mean values were plotted without standard deviations for better readability.

Results

The numerical simulation allowed the determination of ablation shape and size for each treatment parameter set. Simulation results are given in Table 2 and Figure 2 and 3. CT imaging of the ablation zones acquired immediately and 24 hours after the interventional procedure revealed areas of hypoattenuation that were typically composed of a central non-enhancing core and a peripheral zone of moderate contrast enhancement (Figure 1B–D, F–H). Ablation zones appeared well demarcated and distinct from surrounding normally enhancing renal parenchyma. Periablational hyperattenuation compatible with hyperemia of adjacent kidney parenchyma was inconsistently observed. The CT appearance of ablation zones immediately and 24 hours post-procedure was comparable.

CT measurements were obtained from 35 separate ablation zones at two different time points. For all ablation zones, cross sectional areas were calculated from axial CT images parallel to the electrode trajectories including both the central and peripheral zone of the ablation. Mean values for the ablation cross sectional area for all protocol sets and time points are given in Table 2 and Figure 3.

For protocols 1–4 employing two monopolar electrodes ablation zones measured immediately after the intervention were slightly smaller than simulated ablation zones (81±18% of the simulated size, n=24, $p \leq 0.05$) with the relatively (and absolutely) smallest measured ablation zones found for protocol 1 (66±15%, n=10, $p \leq 0.01$), followed by protocol 2 (86±16%, n=3, $p \leq 0.7$), protocol 3 (88±25%, n=5, $p \leq 0.7$) and protocol 4 (99±12%, n=6, $p \leq 0.015$). We observed a significant increase in size for these ablation zones on post-interventional CT follow-ups from day 0 to day 1 by a mean 60±35% (n=24, $p \leq 0.01$). On post-interventional day 1 measured ablation zones were larger than simulated ablation zones (115±18%, n=24, $p \leq 0.089$) with the relatively (and absolutely) largest measured ablation zones found for protocol 3 (128±18%, n=5, $p \leq 0.127$), followed by protocol 4 (116±11%, n=6, $p \leq 0.33$), protocol 2 (112±15%, n=3, $p \leq 0.7$) and protocol 1 (108±21%, n=10, $p \leq 0.7$).

For bipolar electrode settings (protocol 5 and 6) the simulation significantly underestimated the ablation zone as measured on day 0 and day 1 post-interventional CTs. Measured ablation zones were significantly larger than simulated on post-interventional day 0 (190±33%, n=11, $p \leq 0.001$) and day 1 (234±12%, n=11, $p \leq 0.0001$) CT follow-ups.

The cross-sectional shape of the ablation zone on CT corresponded to the simulations (Figure 2), both for bipolar and monopolar electrodes. However, when ablation zones extended into the renal pelvis (n=4) or touched the renal surface focal shape deviations could be observed.

Gross pathology examination of kidneys harvested 24 hours post-ablation revealed well-demarcated hemorrhagic ablation zones. Ablation zones were histologically composed of a central and a peripheral zone (Figure 4). The central zones were characterized by cellular necrosis of all structures including renal tubules, glomeruli and small blood vessels. The peripheral zones were characterized by necrosis of renal tubules only, while glomeruli and blood vessels were viable. Necrosis was characterized by cytoplasmic hypereosinophilia, and nuclear shrinkage (pyknosis), fragmentation (karyorrhexis), or loss (karyolysis), with retention of tissue architecture. Thermal effects could be seen in three ablation zones limited to an area of 40–500 μm adjacent to the electrodes – however, these findings were observed in different protocols and not clearly related to higher energy settings. No differences in histologic ablation effects could be observed related to the location (upper, mid, or lower pole) or the treatment protocol used. For 12 ablation zones two-axis cross sectional measurements were obtained from 24-hour histology slides. Measurements were performed of both the central and peripheral zone of ablation. For corresponding cases two-axis measurements of the central non-enhancing and peripheral enhancing zone were performed on 24 hours CT-scans. Peripheral zones of histologically incomplete ablation measured 3.2±2.5 mm in the long axis and 2.3±2.3 mm in the short axis. Peripheral enhancing zones on CT measured 6.4±1.9 mm in the long axis and 4.1±1.7 mm in the short axis.

An overview of two-axis dimensions of the simulated ablation zone, histology and CT-measurements is given in Table 3. The cross-sectional area of the ablation zone (including the central and peripheral zone) calculated from 2-axis CT measurements significantly exceeded the area calculated from 2-axis histology measurements by a mean 205±113 mm^2 ($p \leq 0.005$). The measured difference was 7±10 mm ($p \leq 0.123$) in the long and 9±6 mm ($p \leq 0.005$) in the short axis diameter. The central non-enhancing area calculated from CT-measurements also significantly exceeded the central area of complete ablation on histology by 100±77 mm^2 ($p \leq 0.007$). The respective differences were 5±8 mm ($p \leq 0.262$) in the long and 6±4 mm ($p \leq 0.005$) in the short axis. Central zones were significantly smaller both for CT (difference of area 154±73 mm^2 ($p \leq 0.003$), long axis 5±5 mm ($p \leq 0.05$), short axis 6±6 mm ($p \leq 0.003$)) and histology (difference of area 49±46 mm2 ($p \leq 0.005$), long axis 3±2 mm ($p \leq 0.005$), short axis 2±2 mm ($p \leq 0.004$)) measurements compared to the respective total ablation zone (including the central and peripheral zone).

Cross-sectional areas of the simulated ablation zones were only slightly larger than the total histologic ablation zone (difference of area 89±94 mm^2, $p \leq 0.047$), while there was no significant difference in long (7±7 mm, $p \leq 0.058$) and short (3±4 mm, $p \leq 0.103$) axis diameters. However, compared to the central area of histologically complete ablation, simulated ablation zones were significantly larger (difference of area 138±85 mm^2 ($p \leq 0.007$), long axis 9±7 mm ($p \leq 0.008$), short axis 7±4 mm ($p \leq 0.009$)).

Discussion

In this study we performed numerical modeling, as it is currently employed in treatment planning for clinical applications of IRE to calculate the ablation size and shape, for different treatment parameter sets and compared simulation results to empiric ablation outcomes of renal IRE from CT and pathology. Treatment parameters were varied within a range previously reported [13, 15] and clinically used [24] to perform kidney IRE. Our results indicate that numerical simulations and empirical ablation outcomes may be different, limiting the reliability of treatment planning for determining IRE ablation size in kidney parenchyma.

Simulations for all studied treatment protocols resulted in smaller ablation zones than measured on 24 hours CT follow-ups, although approximation between measured ablation zones and simulations was better for monopolar than for bipolar electrode configurations. The greater deviation between simulation and CT measurements in the bipolar electrode may be due to the different geometry (featuring two poles on one applicator) and the lower gauge of the bipolar device.

Furthermore, we observed a significant increase in mean ablation size between CT-follow-ups immediately and one day after the intervention. These findings are in line with previous findings that indicate IRE ablation zones may not be fully developed directly after the intervention but rather after 24 hours [25]. The immediate effects of IRE prevalent in the central ablation zone appear to be attributable to necrotic cell death due to loss of homeostasis. Coagulative necrosis of all cellular structures combined with hyperemia and hemorrhage can be observed through H&E stains. However, in the periphery a ring of apoptosis that initiates at the time of ablation and takes 24 hours to complete can be observed [25]. In addition to these effects, there may also be indirect effects due to disruption of local vasculature and immunological response [26]. We therefore considered 24 hours CT measurements more accurate for comparison to simulations than immediate CT measurements.

The ablation effects of IRE could be confirmed by pathology. A dual composition of ablation zones composed of a central zone with complete necrosis of all structures besides peripheral zones with tubular necrosis only and spared vessels and glomeruli was observed on pathology. This dual composition translated into CT findings, which featured a slightly enhancing peripheral zone besides a non-enhancing central zone, most probably due to spared vessels in the ablation zone periphery.

The dual composition of ablation zones suggests that ablation effects in the periphery may be incomplete and that the measured total size of the ablation zone on CT, which included both the central and peripheral zone, may not adequately represent the extent of completely ablated tissue. The peripheral zone may contain incompletely ablated tissue and viable structures. When compared to histology, the peripheral enhancing zone on CT appeared to be slightly larger in width than the peripheral zone of incomplete ablation observed on histology slides. Also the central zone of non-enhancement on CT appeared larger than the central zone of complete ablation measured on histology slides. This observation suggests that CT measurements may overestimate the size of ablation, even if only the central non-enhancing core was considered.

Comparing simulated ablation zones to histology measurements, we observed that, although simulation results more closely approximated histology measurements, they still overestimated the histologic ablation zone, particularly when only the central zone of complete ablation was considered.

Following these observations it may be questioned if a simulation model for planning IRE, which is currently derived from the experience with liver ablations, can be directly translated and reliably used within a different organ such as the kidney. Furthermore, this would implicate that a smaller zone of complete ablation than planned can be expected thus requiring a greater safety margin when employing renal IRE in a clinical setting.

Voltage and electrode spacing were the main parameters determining both the simulated ablation size and the ablation size as measured on CT. The pulse width and the number of pulses applied may have an additional effect, which was not considered in this model as it is not considered in clinical treatment planning. However, since IRE is a threshold phenomenon these treatment parameters are not expected to influence the histologic features of ablation, as long as the critical threshold for IRE ablation is reached within the tissue. One reason for changing pulse parameters while keeping voltage constant is to reduce IRE induced heat generation [27], while maintaining ablation benefits. Cells react in the same way, but the overall increase in conductivity is reduced. This in turn reduces the amount of current drawn thereby mitigating current related Joule heating.

Currently there is no evidence in literature for the exact electric field strength threshold for determining the boundary of IRE in renal tissue. We used a similar threshold as employed in clinical treatment planning (600 V/cm) derived from data reported for liver and soft tissue IRE. However, when compared to outcomes on CT imaging and pathology, where central ablation zones appear to represent complete ablation and peripheral enhancing zones spared glomeruli and vessels, we speculate that this threshold may actually be lower, closer to 500 V/cm.

The mechanism of IRE is based on a cell-death threshold defined through the energy applied to the tissue and there is no graduation of IRE effects, which explains the sharp demarcation between viable and ablated tissue[9, 21]. However, there seems to be a variation of tissue susceptibility and energy thresholds for cell death for different tissues and organ structures. Our observations indicate that tubular epithelium may be more susceptible to IRE ablation than glomerular structures and blood vessels, which were spared in the periphery of the ablation zone, where a reduced electric field density is expected in comparison to the center of ablation. These findings are in line with previous observations in kidney IRE demonstrating no significant impact on kidney perfusion [14]. A clinical liver IRE study [28] has demonstrated that blood vessels in close proximity to IRE ablation zones remain patent using postoperative CT and MRI imaging.

Furthermore, the renal collecting system, which has tissue conductivity values different from the renal cortex, may cause shape deviations of the ablation zone through a conductivity sink effect. Shape deviations of IRE ablation zones through surrounding structures have recently been reported by Ben-David et al. [29]. Thermal effects were observed only in a few ablations and confined to the immediate surroundings of the needle electrodes and were therefore considered insignificant. The majority of literature demonstrates that IRE is a non-thermal technique, although thermal effects are possible and have been described for higher energy settings [27].

This study has limitations. Since no tumor model for swine kidney was available, ablations were performed in healthy animals and on normal kidney tissue. The susceptibility of tumor tissue to IRE ablation may differ from normal healthy tissue due to different electric properties, thus empiric outcomes for tumor ablation are expected to deviate from healthy kidney parenchyma. Thus, further studies will be necessary to establish the value of simulation for IRE ablation in tumor models and in-human application. Apart from the employed method other techniques exist for simulating IRE ablation zones[20], which are, however, still unverified by empiric experimental results. Ablation zones were measured on a cross-sectional plane in two dimensions. Three-dimensional measurements may more accurately represent the effective ablation shape and volume and a z-axis analysis of the ablation volume needs to be addressed in further studies. Due to technical issues histological measurements were obtained from a smaller number of ablation zones than CT measurements, since the full extension of the ablation zone was required to be captured on one histologic slide.

In conclusion, results from simulations as employed in clinical treatment planning for IRE ablations and empirical ablation outcomes in the kidney may differ from each other. Both simulations and CT measurements may overestimate the actual zone of complete tissue ablation in renal IRE as evidenced by histology, which suggests that ablation effects may be incomplete in the periphery of the ablation.

Acknowledgments

Source of Funding: The institution of S. B. Solomon received an unrestricted grant and equipment from Angiodynamics Inc. S. B. Solomon is also a consultant for Covidien and received a grant from GE Healthcare.

References

1. Georgiades CS, Hong K, Bizzell C, et al. Safety and efficacy of CT-guided percutaneous cryoablation for renal cell carcinoma. J Vasc Interv Radiol. 2008; 19:1302–1310. [PubMed: 18725093]
2. Zagoria RJ, Traver MA, Werle DM, et al. Oncologic efficacy of CT-guided percutaneous radiofrequency ablation of renal cell carcinomas. AJR Am J Roentgenol. 2007; 189:429–436. [PubMed: 17646471]
3. Schmit GD, Thompson RH, Kurup AN, et al. Percutaneous cryoablation of solitary sporadic renal cell carcinomas. BJU Int. 2012; 110:526–531.
4. Hui GC, Tuncali K, Tatli S, et al. Comparison of percutaneous and surgical approaches to renal tumor ablation: metaanalysis of effectiveness and complication rates. J Vasc Interv Radiol. 2008; 19:1311–1320. [PubMed: 18725094]
5. Gervais DA, McGovern FJ, Arellano RS, et al. Radiofrequency ablation of renal cell carcinoma: part 1, Indications, results, and role in patient management over a 6-year period and ablation of 100 tumors. AJR Am J Roentgenol. 2005; 185:64–71. [PubMed: 15972400]
6. Gervais DA, Arellano RS, McGovern FJ, et al. Radiofrequency ablation of renal cell carcinoma: part 2, Lessons learned with ablation of 100 tumors. AJR Am J Roentgenol. 2005; 185:72–80. [PubMed: 15972401]
7. Igor Pinkhasov G, Raman JD. Management and prevention of renal ablative therapy complications. World J Urol. 2010; 28:559–564. [PubMed: 20383639]
8. Crow P, Keeley FX. Prevention and handling of complications of renal focal therapies. J Endourol. 2010; 24:765–767. [PubMed: 20377430]
9. Rubinsky B. Irreversible electroporation in medicine. Technol Cancer Res Treat. 2007; 6:255–260. [PubMed: 17668932]
10. Lee RC. Cell injury by electric forces. Ann NY Acad Sci. 2005; 1066:85–91. [PubMed: 16533920]
11. Al-Sakere B, Andre F, Bernat C, et al. Tumor ablation with irreversible electroporation. PLoS One. 2007; 2:e1135. [PubMed: 17989772]
12. Wendler JJ, Pech M, Porsch M, et al. Urinary tract effects after multifocal nonthermal irreversible electroporation of the kidney: acute and chronic monitoring by magnetic resonance imaging, intravenous urography and urinary cytology. Cardiovasc Intervent Radiol. 2012; 35:921–926. [PubMed: 21870207]
13. Deodhar A, Monette S, Single GW Jr, et al. Renal tissue ablation with irreversible electroporation: preliminary results in a porcine model. Urology. 2011; 77:754–760. [PubMed: 21111458]

14. Wendler JJ, Pech M, Blaschke S, et al. Angiography in the isolated perfused kidney: radiological evaluation of vascular protection in tissue ablation by nonthermal irreversible electroporation. Cardiovasc Intervent Radiol. 2012; 35:383–390. [PubMed: 21633883]
15. Wendler JJ, Porsch M, Huhne S, et al. Short- and Mid-term Effects of Irreversible Electroporation on Normal Renal Tissue: An Animal Model. Cardiovasc Intervent Radiol. 2013; 36:512–520. [PubMed: 22893419]
16. Olweny EO, Kapur P, Tan YK, et al. Irreversible electroporation: evaluation of nonthermal and thermal ablative capabilities in the porcine kidney. Urology. 2013; 81:679–684. [PubMed: 23290141]
17. Pech M, Janitzky A, Wendler JJ, et al. Irreversible electroporation of renal cell carcinoma: a first-in-man phase I clinical study. Cardiovasc Intervent Radiol. 2011; 34:132–138. [PubMed: 20711837]
18. Edd JF, Davalos RV. Mathematical modeling of irreversible electroporation for treatment planning. Technol Cancer Res Treat. 2007; 6:275–286. [PubMed: 17668934]
19. Neal RE 2nd, Garcia PA, Robertson JL, et al. Experimental characterization and numerical modeling of tissue electrical conductivity during pulsed electric fields for irreversible electroporation treatment planning. IEEE Trans Biomed Eng. 2012; 59:1076–1085. [PubMed: 22231669]
20. Golberg A, Rubinsky B. A statistical model for multidimensional irreversible electroporation cell death in tissue. Biomed Eng Online. 2010; 9:13. [PubMed: 20187951]
21. Davalos RV, Mir IL, Rubinsky B. Tissue ablation with irreversible electroporation. Ann Biomed Eng. 2005; 33:223–231. [PubMed: 15771276]
22. Daniels C, Rubinsky B. Electrical field and temperature model of nonthermal irreversible electroporation in heterogeneous tissues. J Biomech Eng. 2009; 131:071006. [PubMed: 19640131]
23. Schmidt CR, Shires P, Mootoo M. Real-time ultrasound imaging of irreversible electroporation in a porcine liver model adequately characterizes the zone of cellular necrosis. HPB (Oxford). 2012; 14:98–102. [PubMed: 22221570]
24. Thomson KR, Cheung W, Ellis SJ, et al. Investigation of the safety of irreversible electroporation in humans. J Vasc Interv Radiol. 2011; 22:611–621. [PubMed: 21439847]
25. Kim HB, Sung CK, Baik KY, et al. Changes of apoptosis in tumor tissues with time after irreversible electroporation. Biochem Biophys Res Commun. 2013; 435:651–656. [PubMed: 23688425]
26. Li X, Xu K, Li W, et al. Immunologic response to tumor ablation with irreversible electroporation. PLoS One. 2012; 7:e48749. [PubMed: 23139816]
27. Faroja M, Ahmed M, Appelbaum L, et al. Irreversible electroporation ablation: is all the damage nonthermal? Radiology. 2013; 266:462–470. [PubMed: 23169795]
28. Kingham TP, Karkar AM, D’Angelica MI, et al. Ablation of perivascular hepatic malignant tumors with irreversible electroporation. J Am Coll Surg. 2012; 215:379–387. [PubMed: 22704820]
29. Ben-David E, Ahmed M, Faroja M, et al. Irreversible electroporation: treatment effect is susceptible to local environment and tissue properties. Radiology. 2013; 269:738–747. [PubMed: 23847254]

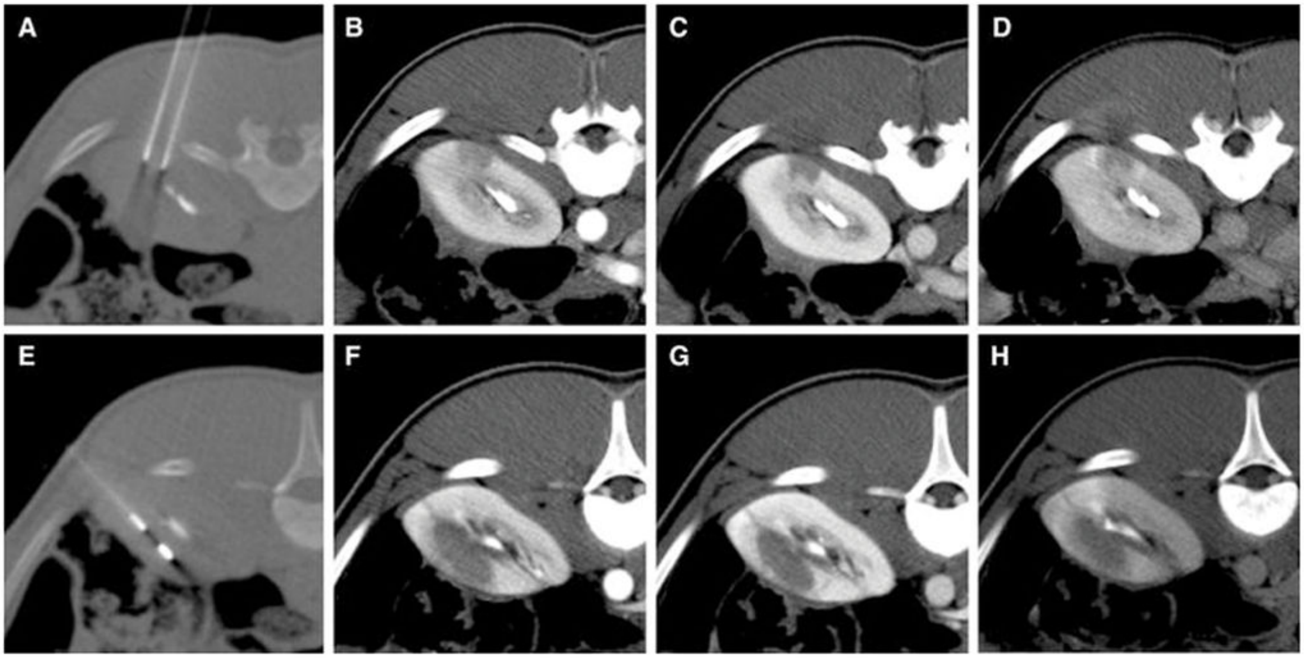

Figure 1.

CT guided electrode placement (A, E) and immediate multiphasic post-interventional CT for a monopolar (protocol 1)(A–D) and a bipolar electrode configuration (protocol 5)(E–H) including arterial (B, F), venous (C, G) and delayed phase (D, H). The collecting system has been contrasted by previous contrast injection for targeting purposes.

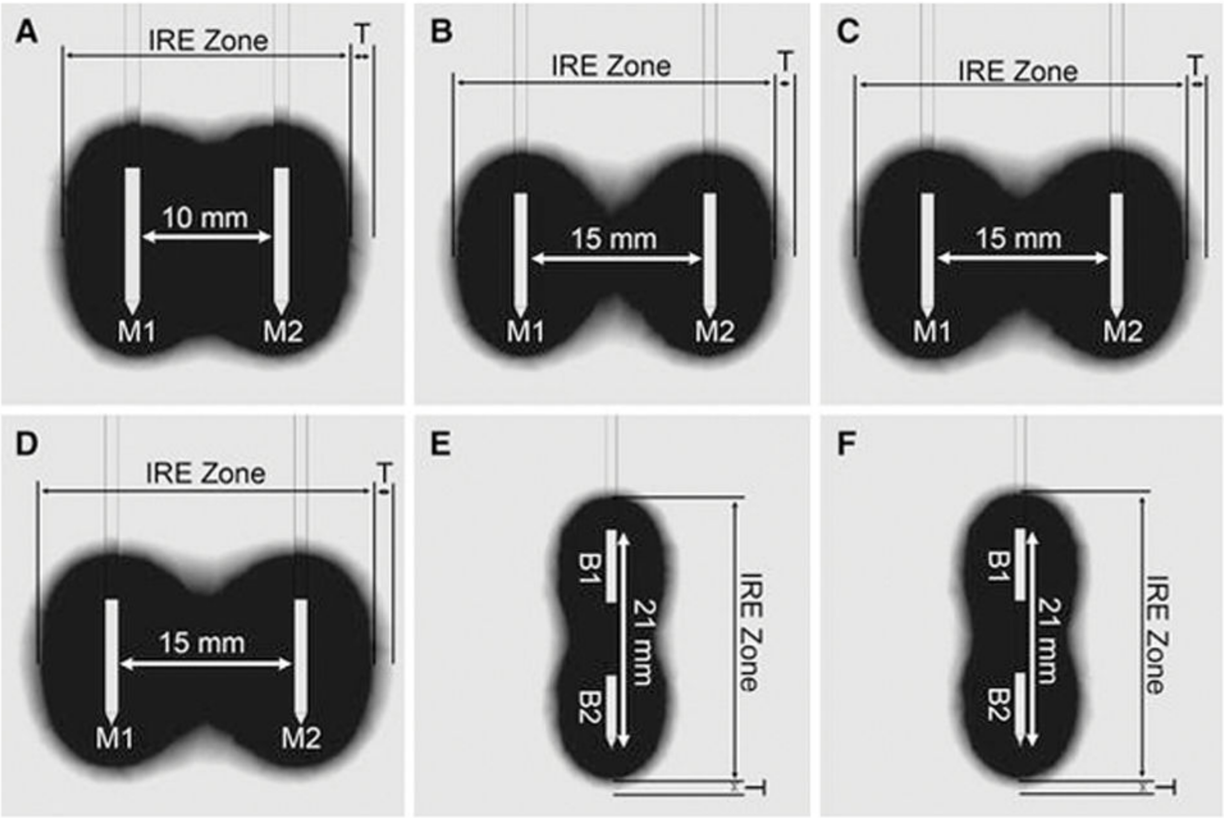

Figure 2.

Results from electrical field modeling showing the simulated ablation zone for monopolar electrode (M1, M2) configurations with 10 mm (A, protocol 1) and 15 mm spacing (B–D, protocol 2–4) and bipolar electrode (B1, B2) configurations (E–F, protocol 5–6). The expected zone of complete ablation (IRE Zone, black) is bordered by a low threshold isovoltaic line of 600 V/cm and a peripheral transition zone (T, greyscales) by a low threshold of 350 V/cm.

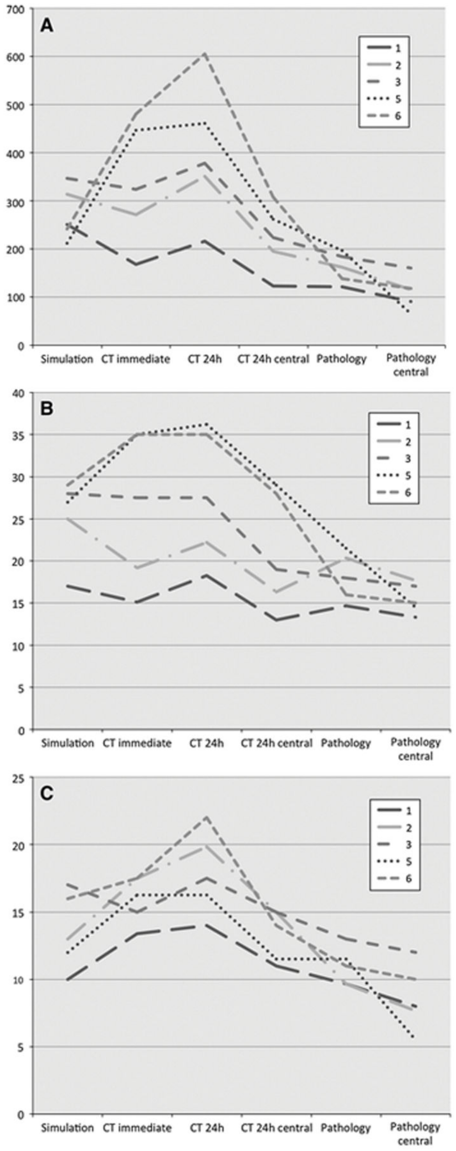

Figure 3.

Comparison of simulated, CT and histopathology measured ablation zones. CT 24h central shows the non-enhancing central zone of ablation. Pathology central shows the central zone of complete ablation. The remaining measurements include central and peripheral zones. Cross-sectional areas [mm^2] (A) were calculated from axial long (B) and short axis (C) measurements [mm].

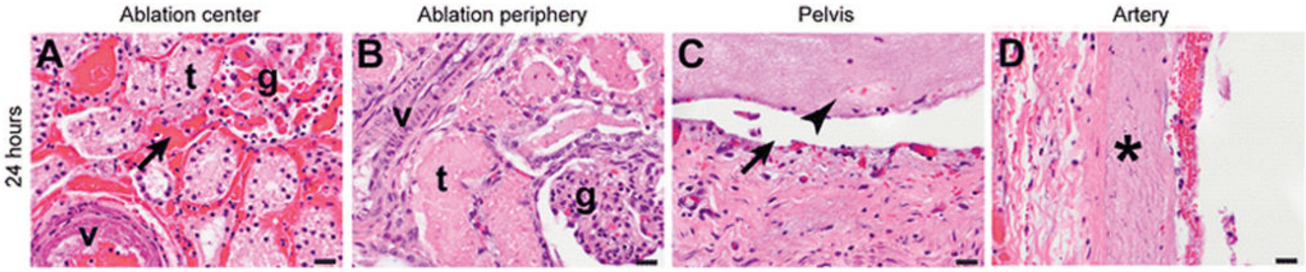

Figure 4.

Histological sections of ablation zones in the kidney. Twenty-four hours after ablation, the center of the ablation zone (A) displays complete necrosis of tubules (t), glomeruli (g), and small blood vessels (v), and hemorrhage (arrow). The periphery (B) displays necrosis of tubules (t) with sparing of glomeruli (g) and small vessels (v), which are viable. The pelvis (C) shows complete loss of epithelium (arrow) and a fibrinous exudate in the lumen (arrowhead). A large artery in the ablation zone (D) shows complete mural necrosis (asterisk). H&E stain. Scale bars: 20 μm.

Table 1

Electrode configurations and pulse settings used for irreversible electroporation.

Protocol Nr.	Ablations (n)	Electrode Type[1]	Spacing[2] [mm]	Exposure[3] [mm]	Voltage [V]	Pulse length [μs]	Pulses (n)
1	10	M	10	10	2000	70	70
2	3	M	15	10	2250	100	70
3	5	M	15	10	2500	100	90
4	6	M	15	10	2700	70	90
5	6	B	N/A	N/A	2400	70	90
6	5	B	N/A	N/A	2700	70	90

[1] M = two monopolar electrodes, B = one bipolar electrode used.

[2] Defines the distance between two monopolar electrodes.

[3] Defines the length of the distal non-insulated part of the electrode.

Table 2

Cross sectional area of the ablation zone derived from [1]numerical simulations for treatment planning and [2]axial CT measurements (x, y). Percentage values are relative to the simulated value. Means and standard deviations are given.

Protocol Nr.	Simulation[1]	CT[2] day 0 [mm^2]	CT[2] day 0 [%]	CT[2] day 1 [mm^2]	CT[2] day 1 [%]
1	251	167±38 *	67±15%	272±53	108±21%
2	314	272±50	87±16%	351±46	112±15%
3	347	305±87	88±25%	444±64	128±18%
4	361	356±45 *	99±12%	417±38	116±11%
5	212	425±48 **	200±23%	491±33 **	232±16%
6	241	430±98	178±41%	576±8 **	239±3%

[*] Area significantly smaller than simulation ($p<0.01$).

[**] Area significantly larger than simulation ($p<0.01$).

Table 3

Twenty-four hours post-ablation size comparison of the [1]simulated ablation zone, the total ablation zone on [2]CT and [3]histology (including central and peripheral zone) and the [4]central non-enhancing ablation zone on CT and the [5]central zone of complete ablation on histology. Mean values in millimeters are given.

Protocol Nr.	**Ablations (n)**	**Simulation[1]**	**CT[2]**	**Histo[3]**	**CT central[4]**	**Histo central[5]**
1	10	17 × 10	18 × 14	15 × 10	13 × 11	13 × 8
2	3	25 × 13	22 × 20	20 × 10	16 × 15	18 × 8
3	5	28 × 17	28 × 18	18 × 13	19 × 15	17 × 12
5	6	27 × 12	36 × 16	22 × 12	29 × 12	15 × 6
6	5	29 × 16	35 × 22	16 × 11	28 × 14	15 × 10